



HAL
open science

A simplified electrochemical model for modelling Li-ion batteries comprising blend and bidispersed electrodes for high power applications

Martin Petit, Elisa Calas, Julien Julien Bernard

► To cite this version:

Martin Petit, Elisa Calas, Julien Julien Bernard. A simplified electrochemical model for modelling Li-ion batteries comprising blend and bidispersed electrodes for high power applications. *Journal of Power Sources*, 2020, 479, pp.228766. 10.1016/j.jpowsour.2020.228766 . hal-02973298

HAL Id: hal-02973298

<https://ifp.hal.science/hal-02973298>

Submitted on 21 Oct 2020

HAL is a multi-disciplinary open access archive for the deposit and dissemination of scientific research documents, whether they are published or not. The documents may come from teaching and research institutions in France or abroad, or from public or private research centers.

L'archive ouverte pluridisciplinaire **HAL**, est destinée au dépôt et à la diffusion de documents scientifiques de niveau recherche, publiés ou non, émanant des établissements d'enseignement et de recherche français ou étrangers, des laboratoires publics ou privés.

A simplified electrochemical model for modelling Li-ion batteries comprising blend and bidispersed electrodes for high power applications

Martin Petit, Elisa Calas, Julien Bernard

IFP Energies Nouvelles, Electrochemistry and Materials department, rond-point de l'échangeur de Solaize, BP3 69360 Solaize, France

Abstract : A fast computing electrochemical model has been developed in order to account for the electrothermal behavior of Li-ion batteries with multiple and/or multidispersed active materials in each electrode. In this study, the cell studied is a high power cell with lithium manganese spinel and lithium cobalt oxide at the positive and Lithium titanate at the negative with 2 particle populations. The model has been calibrated on the said cell and validated on realistic duty profile. It has been then compared against a state-of-the-art Newmann model that showed similar results for both global and inner behavior. However, due to the simplifications adopted for our modelling approach, calculation times of the newly developed model are significantly lower allowing to specific use where fast computing modelling approaches are required. Finally, this model has been used in order to understand the inner behavior of each electrode during constant current charge and discharges as well as hybrid electric vehicle duty cycles and further calculations have been performed to understand the impact of active material repartition in each electrode.

Key-words: Li-ion battery; electrochemical model; titanate; blend electrodes; bidispersed electrode

1. Introduction

As concerns have been growing regarding greenhouse gases emissions of the automotive sector, efforts have been carried out to find ways to electrify vehicles so that their environmental footprint will be reduced. As a consequence, the beginning of the 21st century has seen the development and successful commercialization of hybrid electric vehicles (HEV), plug-in hybrid vehicles (PHEV) and electric vehicles (EV) by almost every car

manufacturer. However, in order to store the energy necessary for the running of these vehicles, fit-for-purpose energy storage systems have been implemented whose characteristics have been adapted to meet the final application demands. This is performed by adjusting the power to energy ratio (P/E) of a given energy storage system with, for instance, high-power battery packs ($P/E > 15$) for HEVs and high-energy battery packs ($P/E < 2$) for EVs.

These performances have been obtained by properly designing the unitary cells composing the battery packs. To do so, cell manufacturers have to choose fit for purpose materials comprising the electrodes and electrolytes, followed by tuning the manufacturing processes in order to get the required electrode thickness and area. To choose the material within electrodes, cell manufacturers have access to a whole range of commercially available positive and negative materials such as lithium ferrous phosphate (LFP), lithium cobalt oxide (LCO), lithium nickel manganese cobalt oxides (NMCs), lithium manganese spinel (LMO), lithium nickel cobalt aluminium oxide (NCA) among other for the positive and for the negative mainly graphite (C) but also lithium titanate (LTO) or more recently silicon (Si). Each of these materials has its own characteristics and response in terms of power and energy although cost, durability and safety are afforded importance. In such cases, it may then become relevant to mix them in order to form blend electrodes [1] in order to obtain a good tradeoff between all these characteristics [2]. Moreover over the past few years, looking for way to increase the specific capacity of negative active materials by using silicon, composite electrode based on graphite and silicon have been investigated in order to mitigate issues related to volumetric expansion [3]. Yet, to guess the final cell performance based on the composition of its electrode is not straightforward, especially when several materials are involved. As a consequence computational modelling is mandatory in order to evaluate the performance of a designed cell prior to the fabrication and assembly of any prototype. Such a model may also provide information on the best cell formulation for a desired set of requirements and can also be used, provided computational costs are low enough, as a reference model to provide realistic cell behavior in more complex simulations at the system level (i.e. the vehicle or the electrical grid stationary storage). Furthermore, experimental investigation of such cells' behavior is very complex and requires the use of model cells that are quite different from commercially available designs. For instance Heubner, Liebman et

al. [4,5] designed a specific experimental setup in order to assess the current repartition between blended materials. This allowed to understand this repartition depending on the material as well as operating conditions. Using fit for purpose modelling tools will reduce cost and permit deeper understanding on the internal response of the cell as well as indicators on how to mitigate observed limitations.

To model the behavior of Li-ion batteries several modelling approaches have been used from the simplest empirical approaches with a quasistatic description of equilibrium voltage and internal resistance or electrical equivalent circuits with RC loops [6,7] which are able to handle dynamic behavior of the resistance. However, these modelling approaches solely rely on the accuracy of their generating experimental database and tend to deliver poor extrapolation results, furthermore when applied to batteries with blend electrode, each material need to be modelled thanks to an electrical equivalent circuit increasing the number of parameter to fit [8]. On the contrary, physics based approaches based on phenomenological description of cell behavior have offer better extrapolation [9]. Newman et al. [10] provided the first mathematical formulation of this model, named pseudo-2-dimensional model (P2D), which served at the time as the ground work of many other modelling studies [11–13]. This model has subsequently been updated in order to take into account the contributions of side reactions such as aging [14–16], and also simplified in order to reduce its computational cost [17–19]. More specifically, Mao et al. [20] developed a multiparticle model in order to assess the behavior of a commercial battery with a blend positive electrode [21]. In this study they analysed the behavior of an electrode composed of LMO, NMC with a bidispersed NMC particle population. Through their model they were able to understand how lithium is transferred amongst NMC and LMO particles when operated. More recently, Carelli et al. [22] have developed a so-called pseudo-3-dimensional model where thermal behavior is taken into account. This has permitted them to assess the behavior of each active material in the positive electrode studied as a function of not only required current but also temperature operating conditions. Based on P2D approaches, this model has high computational costs as for each control volume within the electrode thickness there exist 3 solid particles which are themselves divided into several volume controls as a means of assessing solid diffusion. The objective of this paper is to develop a simplified electrochemical model able to describe the behavior of blended electrodes, with

especially LTO at the negative electrode. Indeed, this negative electrode material is thus suitable for high power applications [23] and recent study from Schröder et al. [24] showed that such material modelling using electrical equivalent circuit is not straightforward. In our case, we investigate 2 different materials in the positive electrode and 1 material in the negative electrode precisely defining the negative electrode active material as a bidispersed material by using 2 populations of particles with nanometric and micrometric particle radii. Our approach is stated as thus; an experimental study will be described, initially, in order to introduce the cell studied and the tests performed that characterize it. Following this, the dedicated modelling approach will be presented and will include the calibration and the values of the model parameters. Finally, the model will be validated and compared to state of the art modelling (P2D) approaches. It will be employed in a simulation in order to discuss the behavior of the different materials present in the electrodes and the influence of electrode design on general cell behaviour.

2. Materials and methods

This study has been carried out on a commercial Li-ion cell which has been tested in order to assess its basic behavior in operation and then dismantled in order to measure and evaluate its component electrodes. Therefore, after briefly describing the studied cell, experimental tests comprising full size tests and post-mortem tests will be presented.

2.1. Tested battery

The tested battery is an EiG T010 10 Ah with a Lithium Titanate (LTO) based negative electrode, with no further details provided on the manufacturer datasheet regarding the chemistry of the positive electrode to its [25]. It is a high power cell dedicated for hybrid electric vehicle applications. Its main characteristics are indicated in Table 1. As this table shows, the modelling has to be able to handle high current pulse power and especially represent the duty cycles that are typical for this cell usage.

Table 1: EiG T010 characteristics

Characteristic	Value
Nominal capacity	10 Ah
Weight	373 g
Nominal voltage	2.4 V
Maximum voltage	3 V

Cut-off voltage	1.5 V
Maximum discharge current (pulse)	200 A (600 A)
Maximum charge current	100 A
Geometry	Pouch cell
Heat exchange area	62 507 mm ²

2.2. Experimental tests

In order to assess their behavior, cells have been submitted to several characterization tests at the IFPEN test facilities. *A priori*, full size tests were performed to evaluate their behavior in operating conditions close to real case usage scenarios, whereas other cells were dismantled for *post-mortem* analysis.

2.2.1. Full size electric tests

In order to assess their nominal operating behavior, full size tests have been performed on the cells using a Digatron power test bench 200 A/50 V associated with a climatic chamber. Significant variables such as voltage, current, temperature have been measured and recorded on a computer during the tests. After warm-up cycling, the cells were submitted to a characterization protocol which consisted of a succession of specific tests such as (i) 1C/1C charge discharge cycles to check cell capacity, (ii) constant current discharge at various rates (from 0.5 A to 200 A), (iii) hybrid pulse power cycle (HPPC) tests [26] and (iv) HEV representative duty cycles where the cell is set successively at 60% and 40% SOC to perform a current duty cycle representative of an HEV vehicle's demands. Such specific and realistic test scenarios have been defined based on the results of a HEV vehicle simulator (from where power profiles were extracted during a Urban Artemis road profile). This protocol is performed at several temperatures from 0°C to 40°C. Such tests were used in order to evaluate the cell performance in nominal conditions. Amongst the tests, constant current discharge tests were performed from 0.5 A to 200 A from 0°C to 40°C. In this protocol, constant current discharge and HPPC tests were conducted to calibrate model parameters whereas representative HEV duty cycles were targeted to validate the model against experimental data.

2.2.2. Post mortem study

In parallel to full size tests, a post mortem study has been conducted on fresh cells on which formation cycles have been performed. These cells have then been dismantled in order to analyze their internal geometry and materials.

2.2.2.1. Structural characterization

Firstly, the cell components (positive and negative electrodes and separator) were separated and measured in order to get separator thickness and electrodes area. Then, electrodes samples from positive and negative were harvested for a physico-chemical analysis on the composition and microstructural properties of the cell. In Figure 1a and b, energy dispersive spectroscopy (EDS) analysis confirms the presence of 2 different materials in the positive electrode. Using X-ray diffraction (XRD), these two materials were determined to be LiMn_2O_4 (LMO) and LiCoO_2 (LCO). By identifying the positions of Co and Mn atoms in Figure 1b, it appears that LCO seems slightly less abundant than LMO. The size of the LCO particles is approximately 10 μm whereas LMO particles are bigger and closer to $\sim 20 \mu\text{m}$. The active layer thickness of the positive electrode is approximately 15 μm . Apart from LMO and LCO, carbon was found through XRD and quantified using flash combustion and gas chromatography with thermal conductivity detector. It consists in small faceted particles, most likely graphite playing the role of conductive additive. The overall weight content of carbon in the positive electrode is 7.1% comprising both carbon from the graphitic additive and the carbon from the binder (PVDF).

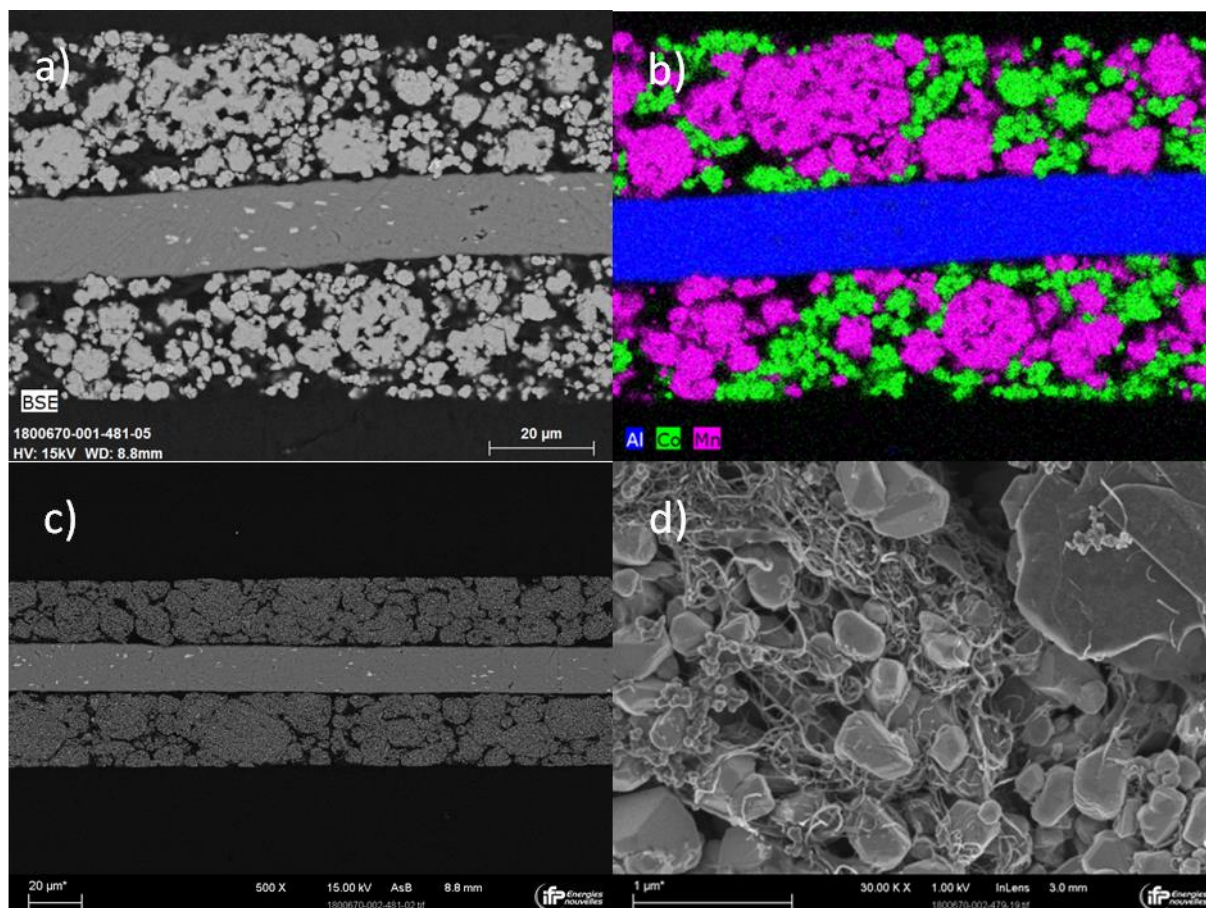


Figure 1: BSE SEM imaging and EDS analysis of positive electrode (resp. a and b) and electronic microscopy analysis of negative electrode (c and d)

Figure 1c and d display cross-sectional and surface imaging of the negative electrode. These analyses combined with X-ray diffraction reveal that the composition of negative electrode was as expected $\text{Li}_4\text{Ti}_5\text{O}_{12}$ with a small amount of carbon (9% weight). As in the positive electrode carbon is present as graphite as well as black carbon. The total amount of carbon comprise graphitic and black carbon as well as carbon used in the binder. The negative electrode active layer is 20 μm thick and is coated by layers comprising small particles (diameter ~ 400 nm) and larger aggregates (~ 10 μm). This confirms the bidispersed nature of the negative electrode particles.

2.2.2.2. Electrochemical tests

Other electrode fragments were harvested in order to perform electrochemical characterization tests. Harvested electrode disks were scraped on one side and then placed in a coin cell with a lithium foil as a negative electrode. Electrochemical tests have been performed using a Bio-logic VMP3 multichannel potentiostatic-galvanostatic system

(BioLogic Science Instruments, France). Tests were performed on half cells mounted with lithium as negative electrode in order to assess single electrode behavior and characteristics. After run-in cycles, and initial checks on the correct behavior of the cells, low current charge and discharge as well as Galvanostatic Intermittent Titration Technique (GITT) tests were performed allowing the precise measurement of electrode equilibrium potential.

However, as the positive electrode is a blended electrode with 2 materials, equilibrium potential of each material is not measurable separately (a mixed potential is measured). Literature expressions were then used in order to assess equilibrium potential of each positive material.

3. Modelling approach

In order to better understand the internal behavior of the cell, a phenomenological physics based modelling approach is chosen. For the cell modelling, an electrochemical model is coupled with a thermal model in order to evaluate the cell electrothermal behavior. Once implemented, this model is calibrated and validated using experimental data.

3.1. Electrochemical modelling

Electrochemical modelling of Li-ion batteries are mostly based on P2D model the fundamental groundwork of Newman et al.. The P2D approach is presented in the top part of Figure 2, and takes into account 2 dimensions in the model; one is the transversal direction from negative to positive electrode dedicated to the solid and electrolyte potentials and electrolyte transport phenomena, the other being the radial direction within the particles dedicated to solid diffusion modelling. Such an approach can be simplified by considering that solid particles are described as single entities as was done by Prada et al. [19] and applied in further studies since [17]. It is a simplified single-particle model with electrolyte modelling (SPM-e), although 2 particles are taken into account in this study (see the bottom part of Figure 2). In this figure, negative and positive electrodes as well as the separator are porous media. As described before, the positive electrode is composed of 2 active materials (LMO and LCO) and the negative electrode is composed of LTO and 2 types of particles, i.e. nano particles and micro aggregates. In order to take into account these specificities, the SPM-e model is adapted to account for each type of material present in the cell:

- in the positive electrode, 1 particle for LMO and 1 particle for LCO
- in the negative electrode, 1 particle for nanosize elements and 1 particle for micro-sized elements both using the same active material, LTO.

For easier reading, i will be used to refer to active materials in the negative; j for active materials in the positive; and k for active materials not specific to either electrode.

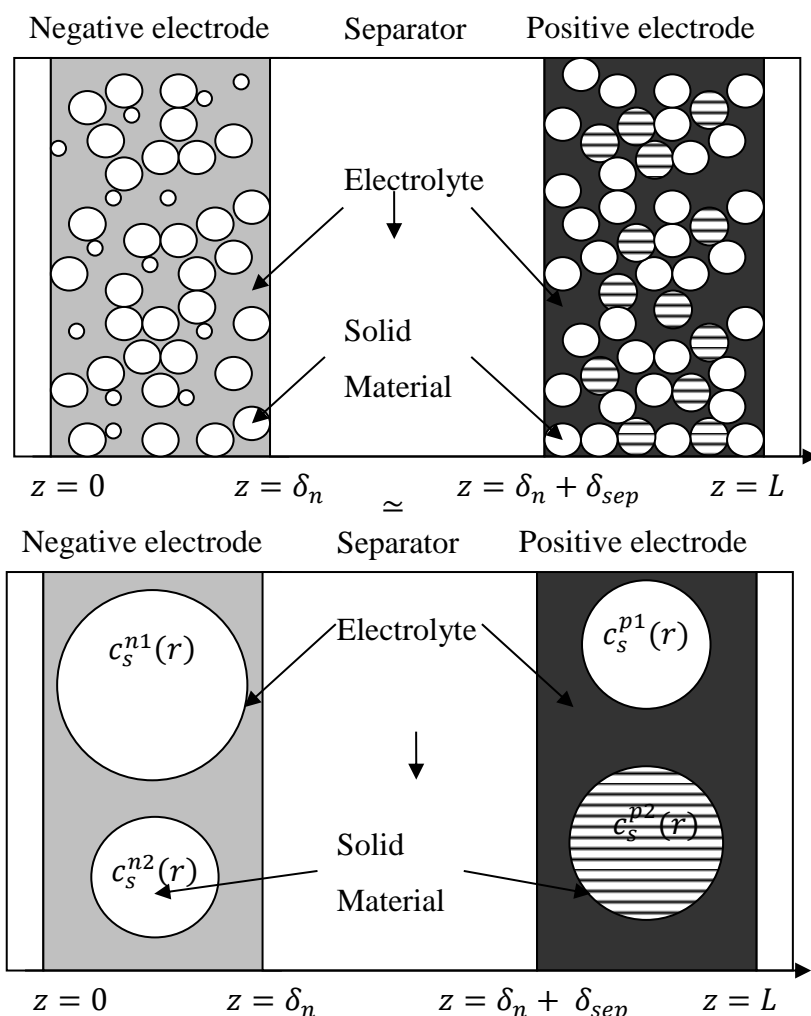
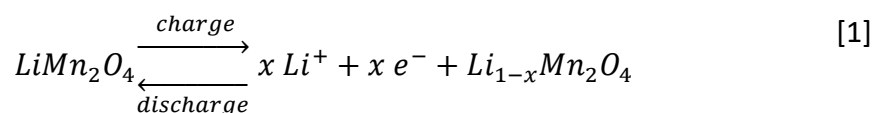
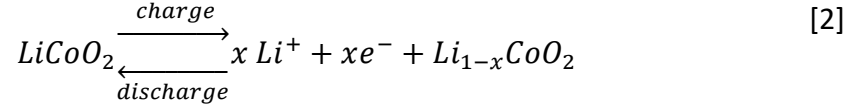


Figure 2: Simplified SPM-e model of a battery with a blend positive electrode and a bidispersed negative electrode (δ_n , δ_{sep} and δ_p are respectively the negative, separator and positive thicknesses, L is the thickness of the electrodes/separator assembly)

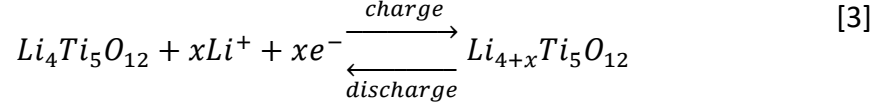
The general electrochemical reactions to be considered for insertion of lithium into positive and negative electrodes are the following:

- at the positive:





- at the negative:



In this model, the main assumptions are that the solid phase can be described by a single particle [19] per material. Therefore, it is supposed that the difference between electrolytic and solid potential, $\Delta\phi = \phi_s - \phi_e$, in both electrodes is uniform. This means that for each active material k there is a single kinetic overvoltage η_{ct}^k . The aim of this model is to evaluate the cell voltage as follows [18]:

$$U_{cell}(t) = \phi_s(L) - \phi_s(0) = \Delta\phi_p - \Delta\phi_n + \eta_s^p - \eta_s^n + \phi_e(L) - \phi_e(0) \quad [4]$$

The modelling approach takes into account the main electrochemical and transport phenomena in such cells [11,17,19]. Mathematical equations describing battery behavior are indicated in Table 2. The phenomena described in this model are the lithium mass conservation inside each particle following Fick's diffusion law (Eq. 9); lithium mass conservation in liquid phase taking into account both diffusion and migration (Eq. 10); (iii) charge conservation in liquid phase (Eq. 12); charge conservation in solid phase (Eq. 11) which is solved analytically in order to evaluate solid ohmic overvoltage η_s in both electrodes (Eq. 20). Electrochemical kinetics are modelled using the Butler-Volmer equation (Eq. 13) and a double layer capacity [12], which develops at both electrode interfaces, and is used to evaluate the difference between solid and electrolytic potentials (Eq. 15).

During battery operation in each electrode, the global electrode current I_{elec} is divided among its constituent particles I_{elec}^k so that:

$$I_{elec} = \sum_k I_{elec}^k \quad [5]$$

For each material modelled, its global current can be evaluated as such:

$$I_{elec}^k = A_{elec} \int_0^{\delta_{elec}} j_f^k(z) dz \quad [6]$$

In this expression A_{elec} is the surface of the electrode in m^2 . Finally, the equilibrium potential of each material U_{elec}^k depends on the concentration at the outermost surface of

the particles and is expressed using the reference potential of the material U_{ref}^k as a function of insertion rate and temperature as follows:

$$U_{elec}^k(t) = U_{ref}^k \left(\frac{c_s^k(R_s^k)}{c_s^{k,max}}, T \right) \quad [7]$$

Transport related equations 9 and 10 are solved using a finite volume method in order to assess the concentration of lithium inside active material particles and in electrolyte. Charge conservation in the electrolyte is solved analytically based on finite volume discretization as in Prada et al. [19] giving the electrolyte overpotential between negative electrode ($z = 0$) and positive electrode ($z = L$) as follows:

$$\phi_e(L) - \phi_e(0) = (1 - t_+) \frac{2RT}{\mathcal{F}} \ln \frac{c_e(L)}{c_e(0)} - \frac{I}{2A_{elec}} \left(\frac{\delta_n}{\kappa_n^{eff}} + 2 \frac{\delta_{sep}}{\kappa_{sep}^{eff}} + \frac{\delta_p}{\kappa_p^{eff}} \right) \quad [8]$$

Table 2: 1D electrochemical model equations [17]

Physical and chemical mechanisms		Eq.	Boundary conditions
Solid phase: conservation of Li^+ species	$\frac{\partial}{\partial t} c_s^k - \frac{1}{r^2} \frac{\partial}{\partial r} \left(r^2 D_s^k \frac{\partial}{\partial r} c_s^k \right) = 0$	[9]	$\begin{aligned} D_s^k \frac{\partial}{\partial r} c_s^k \Big _{r=0} &= 0 \\ -D_s^k \frac{\partial}{\partial r} c_s^k \Big _{r=R_s^k} &= \frac{I_{elec}^k}{a_s^k A_{elec} \delta_{elec} \mathcal{F}} \end{aligned}$
Electrolyte phase: conservation of Li^+ species	$\frac{\partial}{\partial t} \varepsilon^e c^e - \frac{\partial}{\partial z} \left(D_e^{eff} \frac{\partial}{\partial z} c^e \right) - (1 - t_+) \frac{\sum_k j_f^k}{\mathcal{F}} = 0$	[10]	$\frac{\partial}{\partial z} c^e \Big _{z=0} = \frac{\partial}{\partial z} c^e \Big _{z=L} = 0$
Solid phase: charge conservation	$\frac{\partial}{\partial z} \left(\sigma_{eff} \frac{\partial}{\partial z} \phi_s \right) - \sum_k j_f^k = 0$	[11]	$\begin{aligned} -\sigma_{eff}^n \frac{\partial}{\partial z} \phi_s \Big _{z=0} &= -\sigma_{eff}^p \frac{\partial}{\partial z} \phi_s \Big _{z=L} \\ &= I / A_{elec} \\ \frac{\partial}{\partial z} \phi_s \Big _{z=\delta_n} &= \frac{\partial}{\partial z} \phi_s \Big _{z=L-\delta_p} = 0 \end{aligned}$
Electrolyte phase: charge conservation	$\frac{\partial}{\partial z} \left(\kappa_{eff} \frac{\partial}{\partial z} \phi_e \right) + \frac{\partial}{\partial z} \left(\kappa_{eff}^D \frac{\partial}{\partial z} \ln c_e \right) + \sum_k j_f^k(z) = 0$	[12]	$\frac{\partial}{\partial z} \phi_e \Big _{z=0} = \frac{\partial}{\partial z} \phi_e \Big _{z=L} = 0$
Electrochemical kinetics	$\begin{aligned} j_f^i &= a_s^i i_0^i \left(\exp \left(\frac{\alpha \mathcal{F}}{RT} \bar{\eta}_{ct}^i \right) - \exp \left(-\frac{(1-\alpha) \mathcal{F}}{RT} \bar{\eta}_{ct}^i \right) \right) \\ j_f^j &= a_s^j i_0^j \left(\exp \left(\frac{\alpha \mathcal{F}}{RT} \bar{\eta}_{ct}^j \right) - \exp \left(-\frac{(1-\alpha) \mathcal{F}}{RT} \bar{\eta}_{ct}^j \right) \right) \end{aligned}$	[13]	

	$i_0^i = k_0^i c_e^{\alpha_{ox,i}} \left(c_s^{i,max} - c_s^i(R_n^i) \right)^{\alpha_{ox,i}} c_s^i(R_n^i)^{\alpha_{ox,i}}$ $i_0^j = k_0^j c_e^{\alpha_{ox,j}} \left(c_s^{j,max} - c_s^j(R_p^j) \right)^{\alpha_{ox,j}} c_s^j(R_p^j)^{\alpha_{ox,j}}$	
Electrode overpotential	$\bar{\eta}_{ct}^k = \Delta\phi - U_{elec}^k = \bar{\phi}_s - \bar{\phi}_e - U_{elec}^k$	[14]
Double layer capacity	$\frac{d\Delta\phi_p}{dt} = \frac{1}{a_s^p A_{elec} \delta_p C_{dl}^p} \left(I - A_{elec} \int_{L-\delta_p}^L \sum_j j_f^j dz \right)$ $\frac{d\Delta\phi_n}{dt} = \frac{1}{a_s^n A_{elec} \delta_n C_{dl}^n} \left(-I - A_{elec} \int_0^{\delta_n} \sum_i j_f^i dz \right)$	[15]
Electrolyte ionic diffusivity	$D_e^{eff} = D_e \varepsilon_e^{Brugg}$	[16]
Electrolyte ionic conductivity	$\kappa_{eff} = \kappa \varepsilon_e^{Brugg}$	[17]
Electrolyte ionic diffusional conductivity	$\kappa_{eff}^D = \frac{2RT\kappa_{eff}}{\mathcal{F}} (t_+ - 1) \left(1 + \frac{d \ln f_{\pm}}{d \ln c_e} \right)$	[18]
Solid phase electronic conductivity	$\sigma_{eff} = \frac{\sum_k \varepsilon_s^k \sigma_k}{\sum_k \varepsilon_s^k}$	[19]
Solid phase overvoltage	$\eta_s = \frac{I \delta_{elec}}{3 A_{elec} \sigma_{eff}}$	[20]
Specific interfacial surface area	$a_s^k = \frac{3 \varepsilon_s^k}{R_s^k}$	[21]

Since a high power cell is being modelled, fine thermal modelling of the cell is essential. Temperature variation of the cell is evaluated through a simple, lumped thermal model described in Table 3. The energy balance of the cell is described in equation 24. In this equation, temperature evolution is due to the balance between the generated heat flow rate inside the cell (Eq. 25) and the dissipated heat flow rate using a simple heat transfer coefficient h_{conv} in W/m²/K (Eq. 26).

During operation, heat is generated inside the cell through irreversible and reversible heat losses. The two terms involve the cell open circuit voltage OCV and its temperature derivative $\frac{dOCV}{dT}$. Due to the fact that several materials are used in the electrodes, OCV and entropic coefficient $\frac{dOCV}{dT}$ are evaluated as follows:

$$OCV(t) = \sum_j x_j U_p^j(t) - \sum_i x_i U_n^i(t) \quad [22]$$

$$\frac{dOCV}{dT} = \sum_j x_j \frac{dU_p^j}{dT}(t) - \sum_i x_i \frac{dU_n^i}{dT}(t) \quad [23]$$

In these equations, x_i and x_j are the volume fractions of material i in the active material of the negative electrode and the volume fraction of material j in the active material of the positive electrode respectively.

There is a strong coupling between the electrochemical and thermal model since the principal transport and electrochemical reactions parameters such as diffusion coefficients, conductivities and electrochemical reaction rates, are temperature dependent. The electrochemical and thermal models are coupled by using Arrhenius laws for mass transport and kinetics phenomena (Eq. 27) and by using the entropic coefficient as a function of insertion rate x in the evaluation of material equilibrium potential, U_{elec}^k . By using Arrhenius laws, as temperature is increased so do the parameter values. Thus, the overpotential linked to these parameters will be lower at higher temperature.

Table 3. Heat transfer and energy balance equations [19].

Heat transfer and energy balance		Eq.
Energy balance	$\frac{d}{dt}T = \frac{1}{MC_p}(\varphi_{gen} - \varphi_{tra})$	[24]
Thermal flux generated during operation	$\varphi_{gen} = -\left((U_{cell} - OCV_{cell})I + T \frac{dOCV}{dT}I\right)$	[25]
Transferred thermal flux to environment	$\varphi_{tra} = h_{conv}A_{cell}(T - T_{amb})$	[26]
Coupling between 1D electrochemical and lumped thermal models		
Arrhenius law applied to mass transport and kinetic parameters Ψ	$\Psi = \Psi_{ref} \exp\left(\frac{E_a(\Psi)}{R} \left(\frac{1}{T_{ref}} - \frac{1}{T}\right)\right)$	[27]
Temperature dependence of reference potentials as a function of insertion rate x	$U_{elec}^k(x, T) = U_{elec}^k(x, 40^\circ C) + (T - 40) \frac{dU_{elec}^k}{dT}(x)$	[28]

The model has then been implemented in “Simcenter Amesim™”, a software dedicated to system simulation [27]. In order to compare its behavior with a state of the art model, a similar P2D model that considered 2 active materials at each electrode was also implemented in this software.

3.2. Model calibration

The model calibration is based on measurements given by post mortem analysis and literature parameters mainly concerning electrochemical and transport phenomena. Indeed,

some parameters have been fitted to adjust model results to experimental results at cell level. These model parameters are presented in Table 4. When fitted, we have verified that obtained parameters were close in magnitude to previous literature values.

Electrode material equilibrium potentials have been taken from the literature for the positive electrode materials. The LMO equilibrium potential was taken from Mao et al. [20] and the LCO equilibrium potential is taken from Guo et al. [28]. The latter has been slightly modified in order to ensure that the equilibrium potential is very low at full lithiation through the employment of the additional term $\frac{10^{-4}x}{1-x}$ as follows:

$$U_{eq}^{LMO} = 0.225 - 0.392x + 2.2 \tanh(-1010(x - 0.994)) \quad [29]$$

$$+ 1.9 \tanh(-21.4(x - 1.04)) + \frac{0.181}{\cosh(23.4(x - 0.397))}$$

$$- \frac{0.175}{\cosh(24.2(x - 0.399))} + \frac{0.0164}{\cosh(13.1(x - 0.567))}$$

$$+ \frac{0.33}{\cosh(48.1(x - 1))}$$

$$U_{eq}^{LCO} = 4.04596 + \exp(-42.30027x + 16.56714) \quad [30]$$

$$- 0.0488 \operatorname{atan}(50.01833x - 26.48897)$$

$$- 0.05447 \operatorname{atan}(18.99678x - 12.32362)$$

$$- \exp(78.24095x - 78.68074) + \frac{10^{-4}x}{1-x}$$

The entropic coefficient from LMO was taken from Cai et al. [29] and the one for LCO was taken from Guo et al. [28].

The equilibrium potential of LTO electrode is a look-up table based on measurements performed on half-cell with a lithium foil at the negative. The LTO entropic coefficient has been implemented as a look-up table based on the data from Lu et al. [30].

Fitting has been performed using *constant current* charge and discharge cycles with an increasing discharge rate from C/20 to 20C. First, initial stoichiometry as well as positive

material repartition between LMO and LCO were fitted using the C/20 discharge curve. In order to efficiently calibrate this model, results from previous work from Edouard et al. [17] providing a sensitivity analysis of a similar modelling approach have been used. In this study the most sensitive parameters had been identified. As a consequence, parameters automatically fitted were particle radii, electrochemical reactions kinetics, the electrolyte phase diffusion and thenegative nano-particles volume fraction and. Except the last one which was not accounted for in the previous study, all these parameters had a high sensitivity in the study. Electrolyte conductivity, κ_e in S/m, has been derived from Valoen et al. [31] and is expressed as a function of electrolyte concentration c_e in mol/m³ and temperature in K as follows:

$$\kappa_e = (-1.507 \cdot 10^{-2} + 8.808 \cdot 10^{-5}T - 9.48 \cdot 10^{-8}T^2)c_e \quad [31]$$

$$\cdot \exp((-1.58 \cdot 10^{-3} + 7.82 \cdot 10^{-6}T - 1.05 \cdot 10^{-8}T^2) \cdot c_e^{1.217})$$

Table 4. Physical and chemical parameters a 10 Ah LCO-LMO/LTO battery

Parameter	Symbol	Unit	Positive electrode		Separator	Negative electrode	
			Particle 1 LMO	Particle 2 LCO		Particle 1 LTO	Particle 2 LTO
Design specifications							
Electrode thickness	δ	m	2.5 x 10 ⁻⁵ (m)		2.5 x 10 ⁻⁵ (m)	2.5 x 10 ⁻⁵ (m)	
Particle radius	R_s^k	μm	1.94 (a)	0.756 (a)		0.216 (a)	5.3 (a)
Active material volume fraction among active materials	x_k	-	0.62	0.38		0.185	0.815
Active material volume fraction	ε_s	-	0.55 (a)		0.55 (m)	0.42 (a)	
Porosity	ε_e	-	0.33 (a)		0.450 (m)	0.5 (a)	
Filler volume fraction	ε_f	-	0.12 (c)			0.080 (c)	
Double layer capacity	C_{dl}	F/m ²	0.2 [12]			0.2 [12]	
Electrode plate area	A_{elec}	m ²	1.6 x 10 ⁻¹ (m)			1.6 x 10 ⁻¹ (m)	
Solid and electrolyte phase Li ⁺ concentration							
Maximum solid phase concentration	$c_s^{k,max}$	mol m ⁻³	22 860 [32]	51 410 [28]		22 873 [33]	
Stoichiometry at 0% SOC	$x_{0\%}^k$	-	0.977 (a)	0.924 (a)		0.06 (a)	
Transference Number	t^+	-	0.36 [19]				
Average electrolyte concentration at rest	c_e	mol m ⁻³	1 200 [19]				
Bruggman exponent	Brugg	-	1.5		1.5	1.5	
Kinetic and transport properties							
Electrochemical kinetic constant	k^k	-	2.84 x 10 ⁻¹¹ (a)	5.61 x 10 ⁻¹¹ (a)		5.58 x 10 ⁻¹⁰ (a)	
Charge transfer activation energy	$E_{a,ct}^k$	J mol ⁻¹	32 694 (a)	58 000 (a)		20 000 (a)	

Solid phase Li diffusion	D_s^k	$\text{m}^2 \text{s}^{-1}$	1×10^{-13} [32]	1×10^{-14} [28]	1.36×10^{-14} (a)
Solid phase Li diffusion activation energy	$Ea_{diff,s}^k$	J mol^{-1}	31 556 (a)	29 000 [28]	35 000 (a)
Electrolyte phase Li+ diffusion	D_e	$\text{m}^2 \text{s}^{-1}$	4×10^{-11} (a)		
Electrolyte phase Li+ diffusion activation energy	$Ea_{diff,e}$	J mol^{-1}	26 600 (a)		
Electrolyte phase ionic conductivity	κ^{ref}	S m^{-1}	See Eq. 31		
Electronic conductivity reference	σ_0^k	S m^{-1}	1	1	1
Heat transfer coefficient	h_{conv}	$\text{Wm}^{-2}\text{K}^{-1}$			25 (a)
Heat capacity	C_p	$\text{Jkg}^{-1}\text{K}^{-1}$			979 (a)

(a) adjusted

(m) measured

(c) calculated

In order to represent realistic charge and discharge cycles from test benches, the “State Flow Chart interface” from Simcenter Amesim has been used to set the discharge current and perform CC/CV charges. Results from calibration compared to experimental data are shown in Figure 3 (a) and (b). These figures shows that the model is perfectly able to represent the cell behavior during such a test with constant current charges, constant voltage phases, relaxation and variable constant current discharge up until 20C (200A). Voltage relaxation in the model takes place quicker than in experiment, although the final voltage values of relaxation phases are close to those obtained during experimentation. On closer examination (Figure 3 (b)), the model is able to describe precisely constant current discharges until 5C (50 A) with errors lower than 20 mV but overestimates overvoltages at 20C. This shortcoming may be due to the simplified modelling of particle granulometry in the modelling approach. For each electrode, a maximum of 2 particle radii are chosen whereas the distribution of particle sizes in reality is large. Furthermore, it has also been observed that depending on the discharge or charging rate, the apparent radii of active material particles can change [19]. This phenomenon is not completely overcome by using a bidispersed particle distribution in the negative electrode. Still, our model will be used in more realistic tests scenarios.

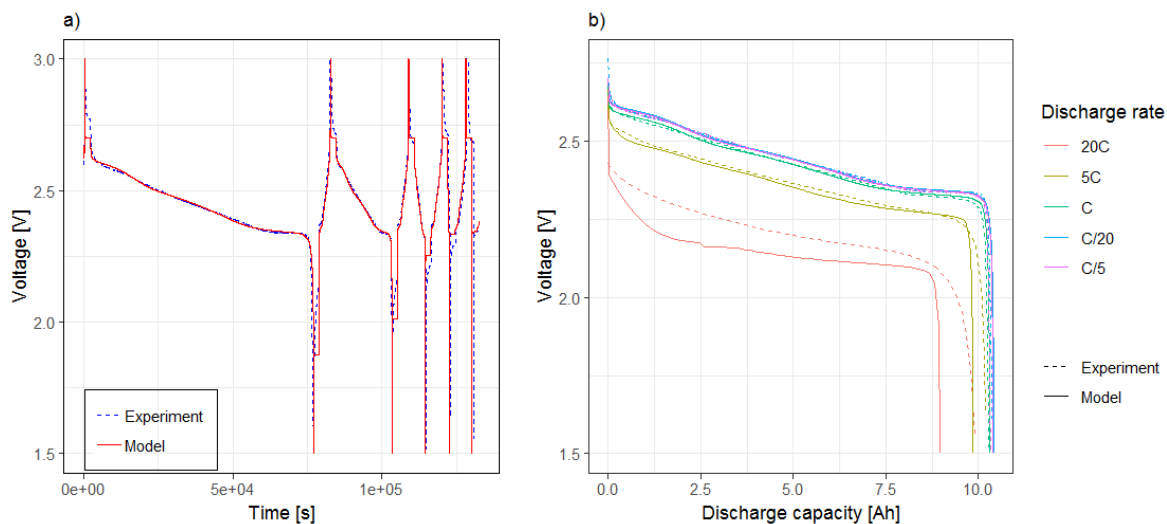


Figure 3: Constant current discharged test modelling results a) Full test simulation, b) detail of discharge results

4. Results and discussion

Having been calibrated, the model still requires validation against other experimental data before being used to predict cell behavior over “out of calibration range” working conditions. Further, it can also be compared to the state of the art model in order to assess its general behavior and validity. Finally, it can be used in order to understand the general functioning of the cell with blended electrodes and to predict cell behavior with other blend compositions.

4.1. Model validation and comparison with the state of the art

As the battery studied is able to handle high power loads, the modelling has been aimed at describing such requirements and validation has been performed by comparing experimental to modelling voltage during a duty cycle representative of HEV loads. During such cycles, SOC stays close to its initial value and high current pulses occur to represent regenerative braking and acceleration phases (from 50 A to -120 A) in the vehicle.

4.1.1. Model performance

Comparison between experimental voltage and model voltage at 25°C are shown in Figure 4. In this figure, which has been obtained without any other parameter fitting after Figure 3 fitting, it can be seen that the model is well able to represent both 1C constant current

charges and discharges with an absolute error lower than 20 mV (as expected from calibration). Furthermore, high frequency solicitations during HEV phases are also well described with an absolute error lower than 15 mV. As a consequence, we consider this model to be well calibrated and fit for purpose for automotive applications.

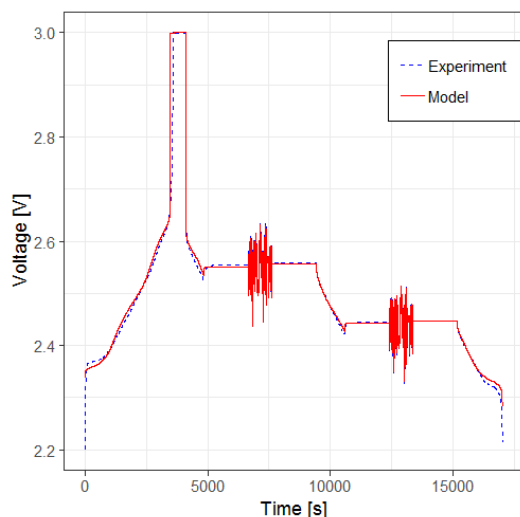
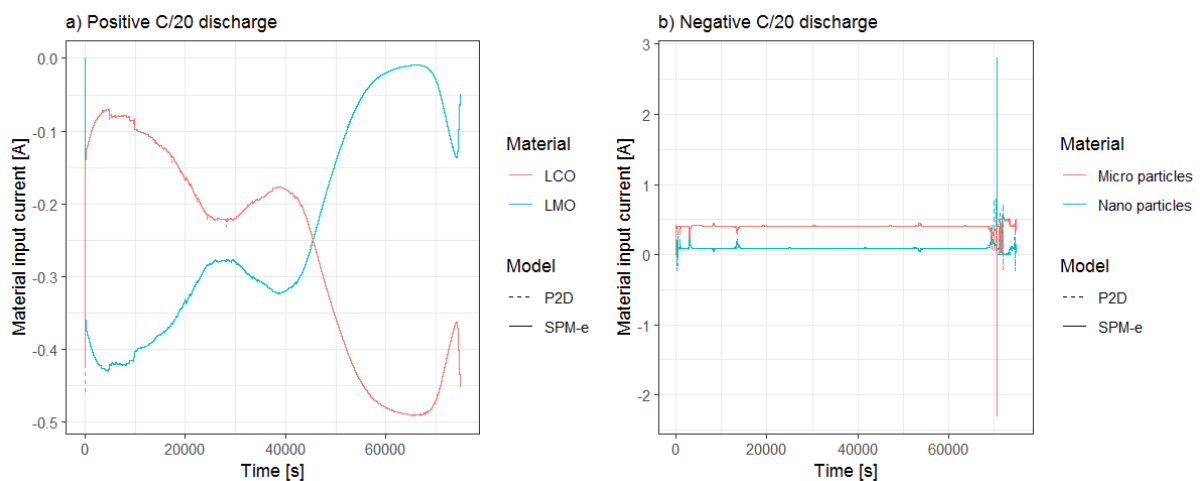


Figure 4: Comparison between experimental and model voltage during a duty cycle representative of HEV demands.

The same parameters have also been applied in a classical P2D model with blend electrodes implemented in Simcenter Amesim. We note that the voltage behavior is very similar between both models, which yield the same absolute error. However, the classical P2D model is far more complex in terms of numerical schemes with 482 state variables whereas the newer SPM-e model comprises only 75 state variables. As a consequence, in order to simulate this 17000s test (on a scientific laptop with a 2,8 GHz Intel® Xeon® CPU and 16 Go RAM) the SPM-e model takes 976 s while the P2D model takes 8600 s. Most computational costs are due to highly dynamic road duty cycles. For simpler constant current charge and discharge cycles, as presented in Figure 3, a 130 000s simulation is performed in 294 s with the SPM-e blend model while it takes almost 9 000 s with the P2D model. With such time-saving benefits, such a model is well suited in order to screen multiple blend composition solutions before prototype production. It may also be embedded within more complex simulations where several other phenomena are to be studied such as current distributions into large cells or aging.

4.1.2. Inner behavior of the cell

The main difference between the classical P2D model and SPM-e model is the fact that the solid phase is considered uniform in the SPM-e whereas there might be differences along the z axis in the P2D model. Figure 5 and Figure 6 show the comparison of input currents of both materials in each electrode. These input currents are the integrated insertion/deinsertion currents along the electrode's length. Their sum equals the total input current of the battery. Results show that for the positive electrode, current repartition between LMO and LCO is very close between P2D and SPM-e models. This can be easily explained by the fact that the electronic conductivity of positive active materials is very high leading to a reduced electronic overvoltage within the positive electrode. As a consequence the positive electrode behavior is almost uniform. However, this behavior tends to change when the discharge current is high. In Figure 5(e), there is a bigger difference between P2D and SPM-e model behavior. At 20C, the solid ohmic overvoltage in the positive electrode is no longer negligible leading to the observed differences.



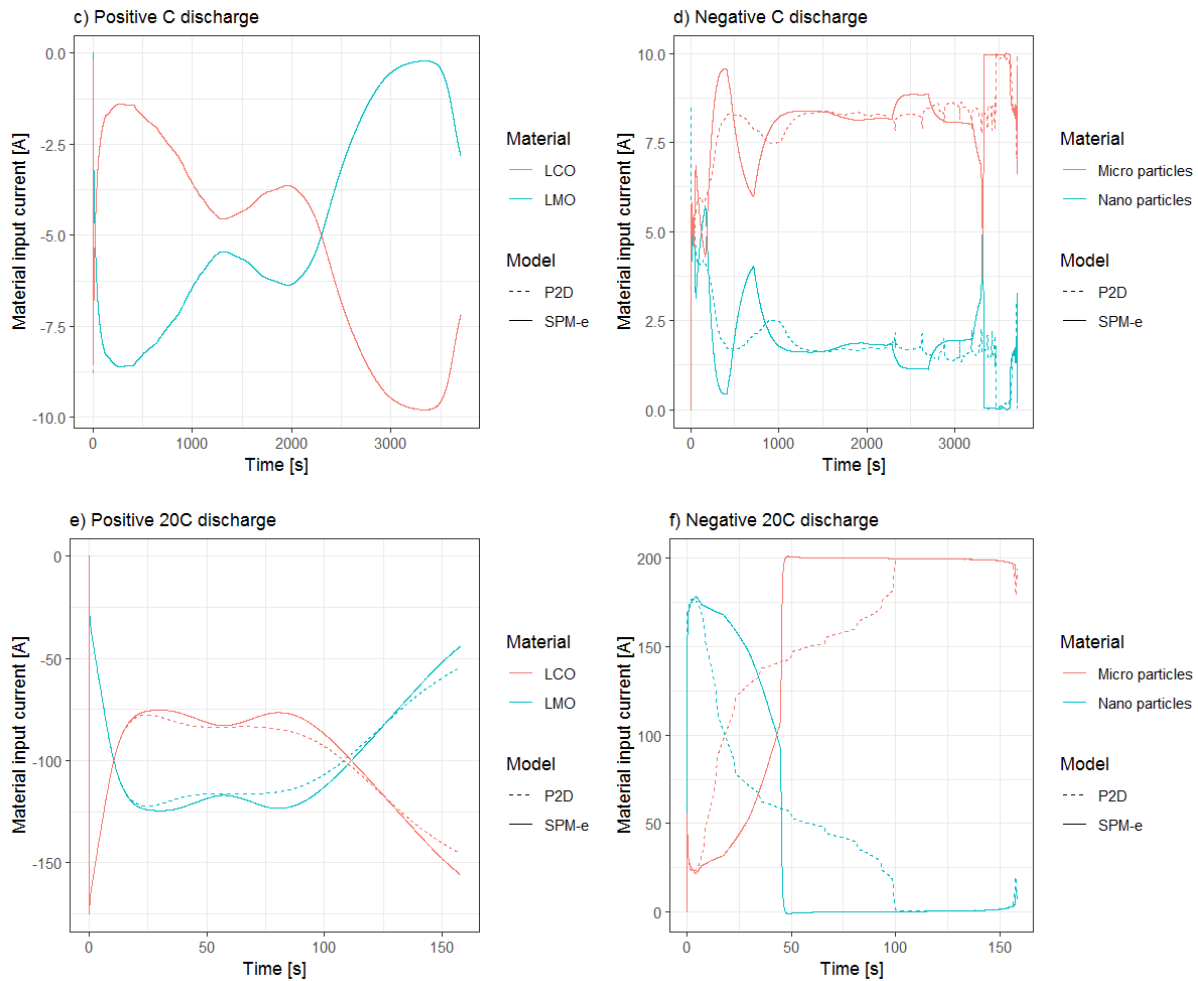


Figure 5: Comparison between input current in positive electrode and input currents in negative electrode among their respective materials during constant current discharge from full charge state

In the negative electrode, the differences are visible at discharge rate as low as 1C. The SPM-e model exhibits sharper current variation amongst the materials when the P2D model current distribution is smoothed. This is due to the fact that the current is not only divided among materials but also along the electrode length. The main differences are visible at high SOC and at low SOC where the equilibrium potential of the LTO slope is very high. In the middle range of the insertion rate, there are very few equilibrium potential variations. As a consequence, current is distributed among the materials following their respective concentration for both models. At the highest discharge rate, differences between SPM-e and P2D model are the biggest.

In Figure 6, same comparison is carried out for higher frequency solicitation during an HEV duty cycles. In the constant current charge and discharge phases, the same trend observed

in Figure 5 are present. During high frequency solicitations, there are almost no differences between P2D and SPM-e models. During these solicitations, overpotentials are mostly due to ohmic drops and there are few variations of electrochemical behavior along the electrode length.

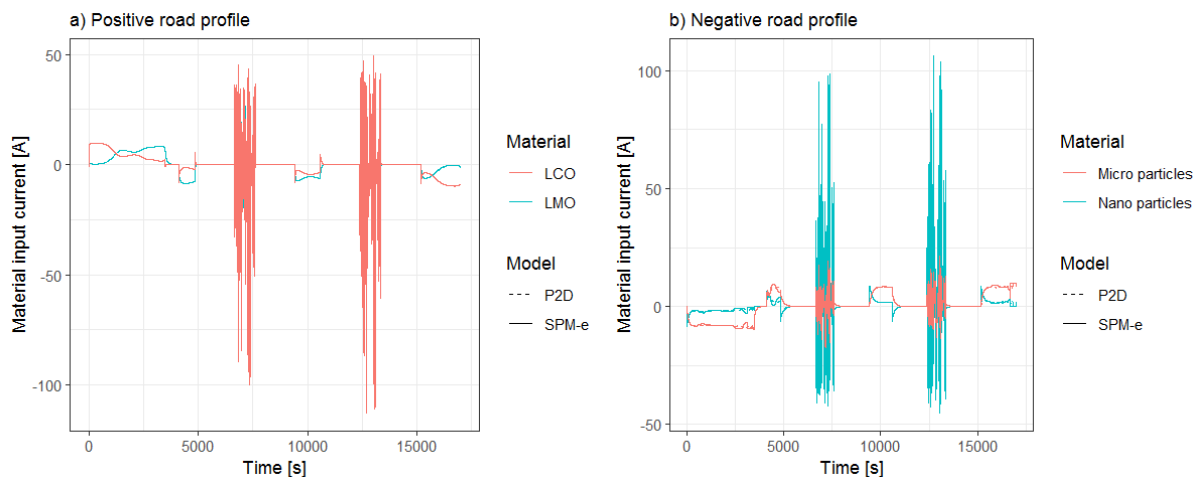


Figure 6: Comparison between input current in positive electrode and input currents in negative electrode among their respective materials during road profile solicitation

4.2. Active material behavior during solicitations

By using the modelling results and especially calculating each material input current, it is possible to assess electrode material performance during loading and which material appears to limit the global cell operation.

4.2.1. Current redistribution between particles during constant current discharge

Depending on operating conditions (current rate, SOH), the redistribution of current will vary between the materials that make up the electrodes. The current will flow in order to ensure that solid potential of all materials stays the same. By looking at Figure 5 and Figure 6, it is possible to understand how it is shared between both positive active materials and negative active materials.

4.2.1.1. Positive electrode

At the positive electrode, there are 2 different materials with different equilibrium potentials. During low rate discharge, the only factor influencing the current repartition is the material potentials. At the beginning of the discharge, around 4V, the equilibrium potential of LMO decrease is lower than that of the LCO. As a consequence, it has to be discharged to a greater extent to arrive at the same potential value as in the LCO. However, at the end of the discharge, the slope of the LCO equilibrium potential becomes lower than the one of LMO. Thus, at the end of discharge, the current flows into the LCO rather than in the LMO.

At the beginning of discharge however, there is always a small period when current is flowing into LMO instead of LCO. This is mainly due to kinetics limitations. In low rate discharge these kinetics limitations are quickly overcome; during high rate discharge (20 C), kinetics limitations do not allow LMO to charge efficiently. As a consequence, during relaxation, LCO discharges into LMO in order to get back balanced equilibrium potentials.

4.2.1.2. Negative electrode

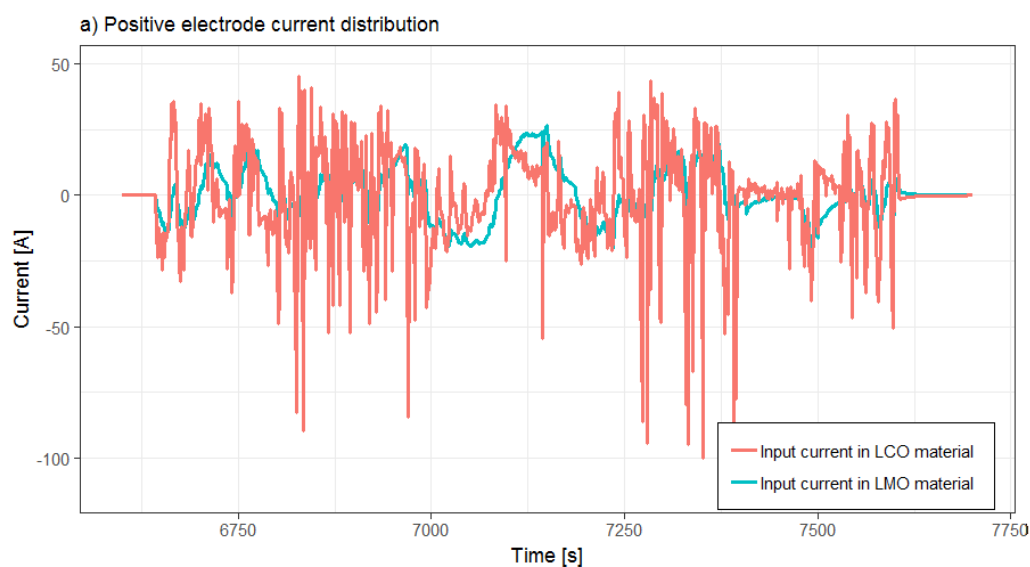
At the negative electrode, there is only 1 material but with 2 different particle sizes. Therefore, only kinetic limitations will play a role here. During low rate discharge (Figure 5b), the current is divided according to the volume fraction of both particle distributions (0.407 A in large particles and 0.093 A in small particles).

With higher discharge rate however (Figure 5d), smaller particles which are easier to charge (higher specific area) are discharged at the beginning of the discharge cycle. As a consequence, by the end of the discharge cycle only the *bigger* particles are affected leading to a larger diffusive limitation since they require longer to transfer lithium from the edge of the particles to the core. This behavior is far more evident when a very high discharge rate is applied (Figure 5f), where small particles are no longer used after 50 s and most of the discharge is handled by bigger particles leading to higher diffusion restrictions and a faster discharge cut-off.

4.2.2. Current distribution between particles during highly dynamic loading

During highly dynamic load cycles (see Figure 6) there are fewer diffusive limitations as the cell keeps being charged and discharged. As a consequence, current repartition is directly linked to the electrochemical kinetics. For the negative electrode (Figure 7b), it means that current flows preferably in the small particles which have a high specific area leading to smaller kinetics overpotentials. Small particles input current presents peaks from 40 A in charge to 95 A in discharge whereas bigger particles' current stays between 20 A in charge and 10 A in discharge. This behavior may prove to be beneficial for the cell's overall performance in aging since bigger particles may be less likely to suffer mechanical stress due to high current ripples.

For the positive electrode (Figure 7a), since LCO has the highest electrochemical reaction rate, it responds with the more dynamic behavior compared to LMO. During highly dynamic loading, it closely follows the cell input current with currents ranging from -90 A in discharge and 40 A in charge. Input current in LMO is smoothed only helping to provide the necessary current during the highest current peaks (112 A at 6826 s) or when the cell stays longer into charge around 7400 s due to increasing diffusive limitations.



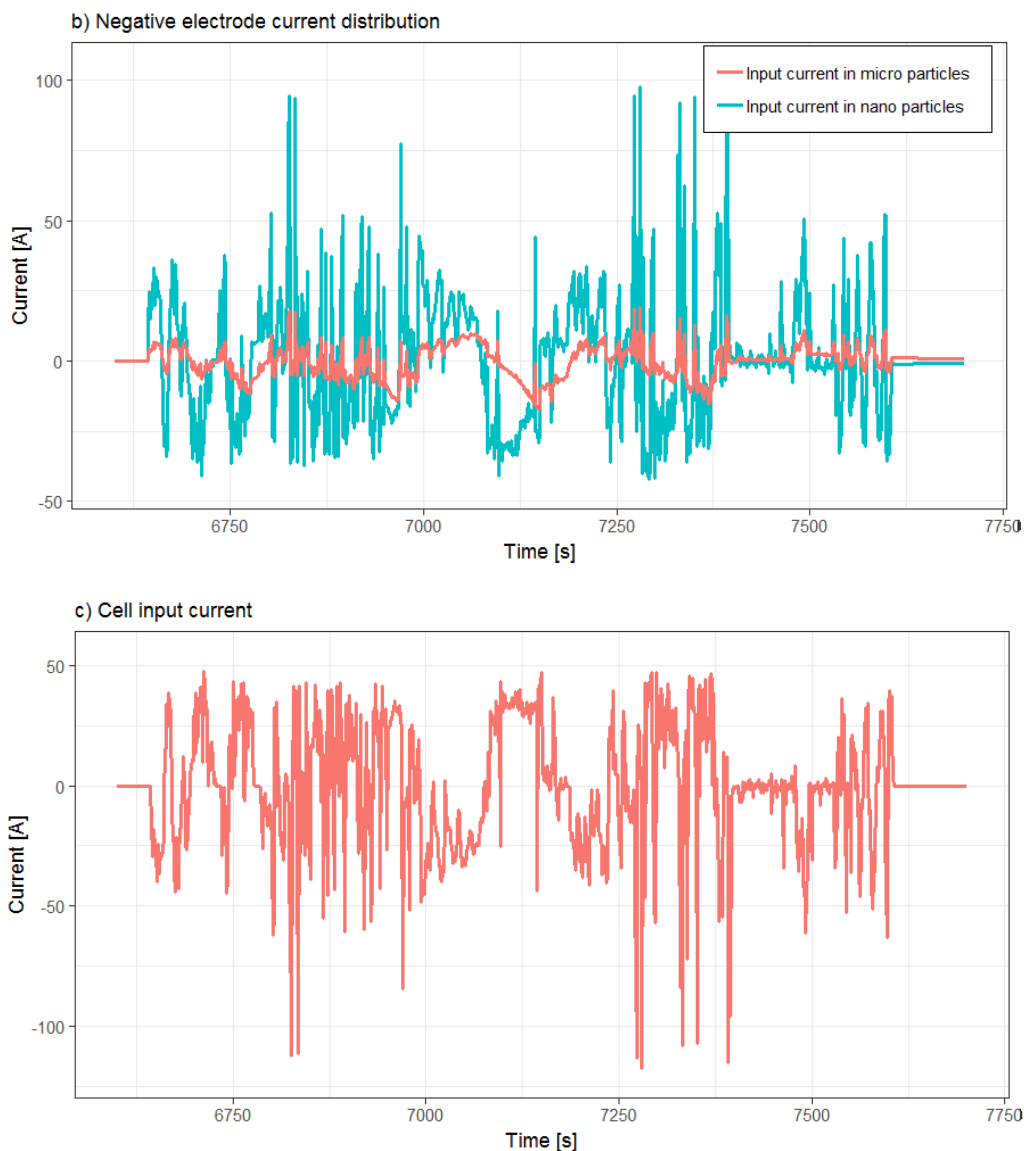


Figure 7: Current repartition during highly dynamic solicitations

This behavior can be related to what has been observed by Heubner et al. [5]. Higher reacting material then constitutes a preferential pathway for the current increasing the overall electrode behavior.

4.3. *Influence of active material choice on cell behavior*

In order to develop better performing cells, the ratio between the materials that make up the electrode may be changed. This may have several effects on both performance (evaluated by employing the model) but also on the cost of the cell by using either cheaper materials (e.g. LMO rather than LCO), or materials that are easier to process (bigger LTO particles).

4.3.1. Balance between positive active materials

First, in order to limit the amount of cobalt in the positive electrode, the volume ratio of LMO may be increased. Simulations have then been performed to assess the capacity as well as the high discharge rate performance of batteries with an increasing volume ratio of LMO from 5% to 95%. At the same time, positive electrode thickness is modified in order to ensure a constant overall capacity of the electrode considering the lithium insertion limits observed using the parameters of Table 4 (0.4 to 0.977 for LMO and 0.5 to 0.924 for LCO). Since capacity density of LMO is lower than the one of LCO, the thickness of the positive electrode with 5% LMO is then lower than the one with 95% LMO. The performance has been assessed by setting the batteries at 0% SOC with 0% stoichiometry $x_{0\%}$ as defined in Table 4. Then, the battery is charged following a 10A CC/CV charge followed by a 1h rest. Finally, the battery is discharged at a constant current rate from 0.5 A to 200 A. The discharge capacity is measured during these discharges. These results are presented in Figure 8a.

For all LMO volume fractions, the discharge capacity decreases with an increasing discharge current. This is a classical behavior due to the higher overvoltages created by high currents. However, it appears also that the capacity for the highest amount of LMO (85% and 95%) in the positive electrode is slightly lower (10.2 Ah) compared to other configurations (10.4 Ah). This behavior should not be accounted for through the amount of active material, as this was addressed through the change in the electrode thickness. Nevertheless, due to the lower electrochemical reaction kinetics of the LMO compared to the LCO, it was not possible to ensure a 1C charge as efficient for the highest LMO content batteries. This leads to a minimum lithium insertion rate of 0.42 in LMO instead of 0.4 in the calibrated cell from Table 4 and 0.35 for a cell with only 5% LMO. As a consequence, the total amount of charge admissible to the positive electrode decreases due to kinetic limitations with higher amount of LMO.

Finally, when all this is considered together, there are very few benefits for having an LMO volume fraction lower than 75% where highest discharge capacities are obtained at lowest discharge currents. On closer inspection, the 75% case is also the one with the calculated maximum discharge capacity at 20C (8.97 Ah from 8.92 Ah with 5% LMO and 8.96 Ah for 97% LMO). This value is close to the one obtained during model calibration. This positive

electrode composition may then have been chosen as a trade-off between cell performance and material cost (considering how expensive the LCO material is).

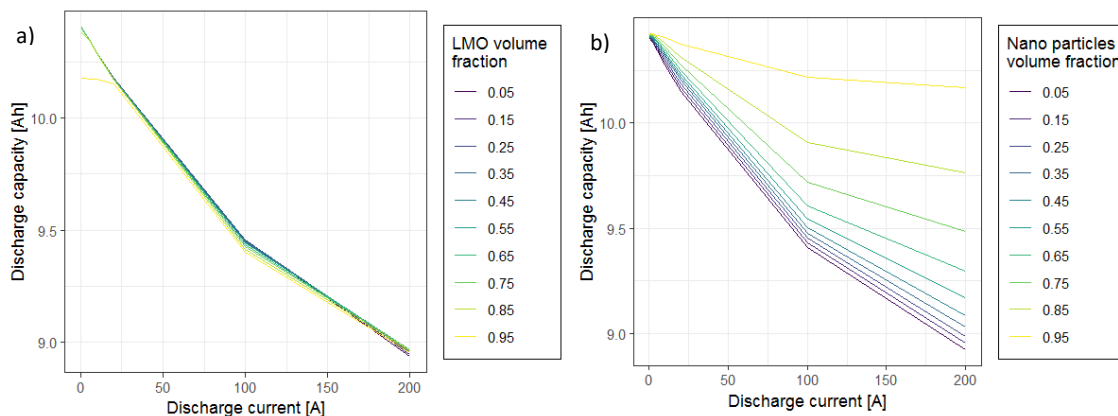


Figure 8: Discharge capacity as a function of the discharge rate for different LMO volume fractions (a) and for different LTO nanoparticles volume fractions (b)

4.3.2. Use of more nanoparticles in the negative

Using the same methodology as before, another parameter sweep has been performed on the nanoparticle volume fraction in the negative electrode. As done in the former section, the performance of the batteries was evaluated in order to assess their capacity as a function of the discharge rate. The results are presented in Figure 8b. Contrary to what was observed in the previous section, there is no change of material between nano and coarse particles. As a consequence, the discharge capacity at low discharge rate is the same for all nanoparticle volume fractions. Yet, as the discharge current increases, the discharge capacity expectedly decreases due to higher overvoltages. For high nanoparticle volume fractions (0.95) the capacity decrease is limited since the specific surface area is far higher through to the smaller particle diameter. As a consequence, for the same volume of active material, the *current density* in the electrode composed of nanoparticles will be lower and the charge transfer overpotential will be lower.

These simulations show the usefulness of controlling/modifying the nanoparticle distribution inside the electrode, keeping all other parameters constant. For instance, increasing the amount of nanoparticles does not change the electrolyte volume fraction and the active material volume fraction in the electrode. In real applications, however, using nano particles

may result in a clogging of electrode porosity leading to a decrease of cell performance that we have not evaluated here.

Explicitly, it is worth noting that 140 simulations have been performed to create Figure 8 using the batch mode of Simcenter Amesim. Four simulations were performed simultaneously and the mean simulation time for each run was 25 s. In total, performing 140 CC/CV charge and constant current discharge took 14 minutes on the same scientific computer as previously mentioned.

5. Conclusions

A simplified physics-based electrochemical SPM-e model has been developed that takes into consideration multiple and bidispersed active materials in the electrodes. This model has then been calibrated and validated against experimental data from a LMO-LCO/LTO 10 Ah commercial cell. This cell has then been modelled using 2 materials at the positive electrode representing each active material observed through experimental tests, and 2 materials at the negative electrode representing 2 particle sizes observed under electronic microscopy. Using this model, we have simulated the behavior of the studied cell and understand its internal behavior during constant current discharge as well as typical HEV loading. In both cases, current redistribution between materials changes depending on the path of least resistance. The more reactive material (higher potential in the positive electrode, and the one with largest reacting area for the negative electrode) is discharged first, as materials return to equilibrium during rest periods.

The SPM-e model was compared to a classical P2D model to assess its performance. For most situations, both behaviors were comparable, although computational times were significantly lower in the novel SPM-e model. The model was also employed to discuss the impact of electrodes composition on cell behavior. Variation of the LMO volume fraction amongst the electroactive materials in the positive electrode showed that using more LCO was beneficial to the cell behavior resulting in a higher cell capacity especially at low discharge rate. One could also observe that below an LMO volume fraction of 0.75, the

improvement in performance became marginal which relates to the actual assessed volume fraction of LMO which is 0.62. For the negative electrode, the use of finer particles during electrode fabrication may offer better behavior in terms of power capability despite the inherent manufacturing limitations which were not assessed in our study.

We believe that the SPM-e model is well suited for the design of composite electrodes of Li-ion batteries. Since its computation time is low, it can be used to evaluate the long term performance of batteries by taking aging into account. Coupled with physical aging models, it could be particularly indicated to take into account specific aging behavior where there is different degradation kinetics among materials of a blended electrode or to assess the growth of a new material such as Li plated on graphitic negative electrode. Furthermore, with the development of Si based negative electrode, this modelling can describe interactions between Si and graphite and the effect of degradation occurring especially in Si particles. It may also be coupled with a 3D thermal model and a 3D electric model to assess the current distribution inside Li-ion batteries and its consequences on batteries performances.

It is also possible to use this approach comprising multiple reactions and a double layer capacity in other contexts of electrochemical reactors such as flow batteries. Indeed, multiple electrochemical reactions may take place like in the first charge of vanadium flow batteries where V^{III}/V^{IV} reaction competes with V^{II}/V^{III} reaction at the negative and with V^{IV}/V^{V} at the positive or where main reaction may also compete with hydrogen or oxygen reaction in aqueous electrolytes.

Acknowledgements

The authors would like to acknowledge Dr Gaurav JOSHI for his advices and his skilled proof-reading of this paper.

6. References

- [1] S.B. Chikkannavar, D.M. Bernardi, L. Liu, A review of blended cathode materials for use in Li-ion batteries, *J.Power Sources* 248 (2014) 91–100.

- [2] P. Albertus, J. Christensen, J. Newman, Experiments on and Modeling of Positive Electrodes with Multiple Active Materials for Lithium-Ion Batteries, *J. Electrochem. Soc.* 156 (7) (2009) A606. <https://doi.org/10.1149/1.3129656>.
- [3] J. Kirner, Y. Qin, L. Zhang, A. Jansen, W. Lu, Optimization of Graphite–SiO blend electrodes for lithium-ion batteries: Stable cycling enabled by single-walled carbon nanotube conductive additive, *Journal of Power Sources* 450 (2020) 227711. <https://doi.org/10.1016/j.jpowsour.2020.227711>.
- [4] T. Liebmann, C. Heubner, C. Lämmel, M. Schneider, A. Michaelis, Investigations on the Effective Electric Loads in Blended Insertion Electrodes for Lithium - Ion Batteries, *ChemElectroChem* 6 (22) (2019) 5728–5734. <https://doi.org/10.1002/celec.201901554>.
- [5] C. Heubner, T. Liebmann, C. Lämmel, M. Schneider, A. Michaelis, Internal dynamics of blended Li-insertion electrodes, *Journal of Energy Storage* 20 (2018) 101–108. <https://doi.org/10.1016/j.est.2018.09.003>.
- [6] E. Prada, J. Bernard, R. Mingant, V. Sauvant-Moynot, Li-ion thermal issues and modeling in nominal and extreme operating conditions for HEV/PHEV's, in: 2010 IEEE Vehicle Power and Propulsion Conference Lille, France September 1-3, 2010, Lille, France, Piscataway, NJ, 2010.
- [7] J. Bisquert, G. Garcia-Belmonte, P. Bueno, E. Longo, L.O.S. Bulhões, Impedance of constant phase element (CPE)-blocked diffusion in film electrodes, *J. Electroanal. Chem.* 452 (2) (1998) 229–234. [https://doi.org/10.1016/S0022-0728\(98\)00115-6](https://doi.org/10.1016/S0022-0728(98)00115-6).
- [8] A. Rodríguez, G.L. Plett, Controls-oriented models of lithium-ion cells having blend electrodes. Part 1: Equivalent circuits, *Journal of Energy Storage* 11 (2017) 162–177. <https://doi.org/10.1016/j.est.2017.02.004>.
- [9] A. Rodríguez, G.L. Plett, Controls-oriented models of lithium-ion cells having blend electrodes. Part 2: Physics-based reduced-order models, *Journal of Energy Storage* 11 (2017) 219–236. <https://doi.org/10.1016/j.est.2017.02.006>.
- [10] J. Newman, W. Tiedemann, Porous-electrode theory with battery applications, *AIChE J.* 21 (1) (1975) 25–41. <https://doi.org/10.1002/aic.690210103>.
- [11] K. Smith, C.Y. Wang, Power and thermal characterization of a lithium-ion battery pack for hybrid-electric vehicles, *J. Power Sources* 160 (1) (2006) 662–673.

- [12] N. Legrand, S. Raël, B. Knosp, M. Hinaje, P. Desprez, F. Lopicque, Including double-layer capacitance in lithium-ion battery mathematical models, *J. Power Sources* 251 (2014) 370–378. <https://doi.org/10.1016/j.jpowsour.2013.11.044>.
- [13] M. Safari, C. Delacourt, Modeling of a Commercial Graphite/LiFePO₄ Cell, *J. Electrochem. Soc.* 158 (5) (2011) A562–A571.
- [14] X.-G. Yang, Y. Leng, G. Zhang, S. Ge, C.-Y. Wang, Modeling of lithium plating induced aging of lithium-ion batteries: Transition from linear to nonlinear aging, *Journal of Power Sources* 360 (2017) 28–40. <https://doi.org/10.1016/j.jpowsour.2017.05.110>.
- [15] E. Prada, D. Di Domenico, Y. Creff, J. Bernard, V. Sauvant-Moynot, F. Huet, A Simplified Electrochemical and Thermal Aging Model of LiFePO₄-Graphite Li-ion Batteries: Power and Capacity Fade Simulations, *J. Electrochem. Soc.* 160 (4) (2013) A616–A628. <https://doi.org/10.1149/2.053304jes>.
- [16] M. Safari, C. Delacourt, Simulation-Based Analysis of Aging Phenomena in a Commercial Graphite/LiFePO₄ Cell, *J. Electrochem. Soc.* 158 (12) (2011) A1436–A1447.
- [17] C. Edouard, M. Petit, C. Forgez, J. Bernard, R. Revel, Parameter sensitivity analysis of a simplified electrochemical and thermal model for Li-ion batteries aging, *J. Power Sources* 325 (2016) 482–494. <https://doi.org/10.1016/j.jpowsour.2016.06.030>.
- [18] D. Di Domenico, A. Stefanopoulou, G. Fiengo, Lithium-Ion Battery State of Charge and Critical Surface Charge Estimation Using an Electrochemical Model-Based Extended Kalman Filter, *J. Dyn. Sys., Meas., Control (Journal of dynamic systems, measurement, and control)* 132 (6) (2010) 061302-1-061302-11. <https://doi.org/10.1115/1.4002475>.
- [19] E. Prada, D. Di Domenico, Y. Creff, J. Bernard, V. Sauvant-Moynot, F. Huet, Simplified Electrochemical and Thermal Model of LiFePO₄-Graphite Li-Ion Batteries for Fast Charge Applications, *J. Electrochem. Soc.* 159 (9) (2012) A1508–A1519. <https://doi.org/10.1149/2.064209jes>.
- [20] Z. Mao, M. Farkhondeh, M. Pritzker, M. Fowler, Z. Chen, Multi-Particle Model for a Commercial Blended Lithium-Ion Electrode, *J. Electrochem. Soc.* 163 (3) (2015) A458–A469. <https://doi.org/10.1149/2.0321603jes>.
- [21] Z. Mao, M. Farkhondeh, M. Pritzker, M. Fowler, Z. Chen, Dynamics of a Blended Lithium-Ion Battery Electrode During Galvanostatic Intermittent Titration Technique, *Electrochimica Acta* 222 (2016) 1741–1750. <https://doi.org/10.1016/j.electacta.2016.11.169>.

- [22] S. Carelli, M. Quarti, M.C. Yagci, W.G. Bessler, Modeling and Experimental Validation of a High-Power Lithium-Ion Pouch Cell with LCO/NCA Blend Cathode, *J. Electrochem. Soc.* 166 (13) (2019) A2990-A3003. <https://doi.org/10.1149/2.0301913jes>.
- [23] N. Nitta, F. Wu, J.T. Lee, G. Yushin, Li-ion battery materials: present and future, *Materials Today* 18 (5) (2015) 252–264.
- [24] P. Schröer, H. van Faassen, T. Nemeth, M. Kuipers, D.U. Sauer, Challenges in modeling high power lithium titanate oxide cells in battery management systems, *Journal of Energy Storage* 28 (2020) 101189. <https://doi.org/10.1016/j.est.2019.101189>.
- [25] EiG, ePLB T Super Power Product: T010, 2015. <https://www.komachine.com/vi/companies/eig/products/56932-T010/> (accessed 16 October 2019).
- [26] FreedomCAR Program Electrochemical Energy Storage Team, FreedomCar Battery Test Manual For Power-assist hybrid Electric vehicle, 2003.
- [27] Siemens Digital Industry Software, Simcenter Amesim, 2017. <https://www.plm.automation.siemens.com/global/fr/products/simcenter/simcenter-amesim.html>.
- [28] M. Guo, G. Sikha, R.E. White, Single-Particle Model for a Lithium-Ion Cell: Thermal Behavior, *J. Electrochem. Soc.* 158 (2) (2011) A122-A132. <https://doi.org/10.1149/1.3521314>.
- [29] Y. Dai, L. Cai, R.E. White, Capacity Fade Model for Spinel LiMn₂O₄ Electrode, *J. Electrochem. Soc.* 160 (1) (2013) A182-A190. <https://doi.org/10.1149/2.026302jes>.
- [30] W. Lu, I. Belharouak, J. Liu, K. Amine, Thermal properties of Li₄/3Ti₅/3O₄/LiMn₂O₄ cell, *Journal of Power Sources* 174 (2) (2007) 673–677. <https://doi.org/10.1016/j.jpowsour.2007.06.199>.
- [31] L.O. Valóén, J.N. Reimers, Transport Properties of LiPF₆-Based Li-Ion Battery Electrolytes, *J. Electrochem. Soc.* 152 (5) (2005) A882. <https://doi.org/10.1149/1.1872737>.
- [32] M. Doyle, Comparison of Modeling Predictions with Experimental Data from Plastic Lithium Ion Cells, *J. Electrochem. Soc.* 143 (6) (1996) 1890. <https://doi.org/10.1149/1.1836921>.

- [33] A.G. Kashkooli, G. Lui, S. Farhad, D.U. Lee, K. Feng, A. Yu, Z. Chen, Nano-particle size effect on the performance of $\text{Li}_4\text{Ti}_5\text{O}_{12}$ spinel, *Electrochimica Acta* 196 (2016) 33–40. <https://doi.org/10.1016/j.electacta.2016.02.153>.